Chemical Science

ROYAL SOCIETY OF CHEMISTRY

EDGE ARTICLE

View Article Online
View Journal | View Issue

Cite this: *Chem. Sci.*, 2021, **12**, 9742

All publication charges for this article have been paid for by the Royal Society of Chemistry

Coexistence of magnetic and electric orderings in a divalent Cr^{2+}-based multiaxial molecular ferroelectric†

Yong Ai, ‡[a] Rong Sun,‡[b] Yu-Ling Zeng,[a] Jun-Chao Liu,[a] Yuan-Yuan Tang,[a] Bing-Wu Wang,[b] Zhe-Ming Wang,[b] Song Gao *[b] and Ren-Gen Xiong *[a]

Received 3rd April 2021
Accepted 14th June 2021

DOI: 10.1039/d1sc01871j

rsc.li/chemical-science

Multiferroic materials have attracted great interest because of their underlying new science and promising applications in data storage and mutual control devices. However, they are still very rare and highly imperative to be developed. Here, we report an organic–inorganic hybrid perovskite trimethylchloromethylammonium chromium chloride (TMCM–$CrCl_3$), showing the coexistence of magnetic and electric orderings. It displays a paraelectric–ferroelectric phase transition at 397 K with an Aizu notation of 6/*mFm*, and spin-canted antiferromagnetic ordering with a Néel temperature of 4.8 K. The ferroelectricity originates from the orientational ordering of TMCM cations, and the magnetism is from the $[CrCl_3]^-$ framework. Remarkably, TMCM–$CrCl_3$ is the first experimentally confirmed divalent Cr^{2+}-based multiferroic material as far as we know. A new category of hybrid multiferroic materials is pointed out in this work, and more Cr^{2+}-based multiferroic materials will be expectedly developed in the future.

Introduction

Ferroelectric materials, which involve a variety of substances containing inorganic ceramics, organic compounds, and organic–inorganic hybrids, have long attracted enormous attention for their technological applications in transducers, capacitors, sensors, *etc.*[1–6] By comparison, multiferroic materials simultaneously possess at least two ferroic orders in a single phase. The coexistence of magnetic order and ferroelectricity is especially attractive for their underlying scientific significance and promising applications in multistate data storage and signal process.[7–9] However, multiferroics have been very rare to date, and the most studied ones are inorganic transition-metal oxides,[10–13] such as $BiFeO_3$,[14] $BiMnO_3$,[15] $RMnO_3$ (R = rare earth elements),[16] and $TbMn_2O_5$,[17] because the mutual exclusion between ferroelectricity and magnetism makes this combination so challenging to achieve. In general, magnetism usually results from the ordered spins of electrons in the partially filled d orbitals of transition metals, while ferroelectricity requires residual polarization from a stable off-centred ion with empty d shells.[18–21] To address this contradiction, the research has been extended to organic–inorganic hybrid frameworks in an attempt to open up a new avenue to multiferroic behaviour.

In organic–inorganic hybrid ferroelectrics, the polar electric ordering generally originates from the ordering alignments associated with organic components.[22–24] Beyond conventional inorganic materials, hybrid ones that merge the benefits of both organic molecules and inorganic skeletons are promising candidates for various multifunctional materials.[25–28] Most of the discovered and theoretically predicted hybrid multiferroics are a series of three-dimensional metal–organic frameworks, represented by [ammonium][$M(HCOO)_3$], where M^{2+} is a transition-metal ion such as Cu^{2+}, Mn^{2+}, Fe^{2+} and Ni^{2+}.[29–33] The magnetism and ferroelectricity in these compounds have different origins: the magnetism derives from the $[M(HCOO)_3]^-$ framework while the ferroelectric order is attributed to the order–disorder transition associated with organic components. However, currently reported organic–inorganic hybrid multiferroics are even rarer than inorganic oxides, and the material diversity is greatly restricted despite other new sporadic cases being reported.[32–42] In this context, it is highly imperative to develop new types of hybrid multiferroics. In an attempt to open up a new avenue of multiferroic materials, we have investigated compounds of Cr in its (unusual) divalent state. Stroppa *et al.* had theoretically predicted that a Cr^{2+}-based perovskite $[C(NH_2)_3][Cr(HCOO)_3]$ might be a new multiferroic, while it had not been successfully synthesized.[43]

[a]*Ordered Matter Science Research Center, Nanchang University, Nanchang 330031, P. R. China. E-mail: xiongrg@seu.edu.cn*

[b]*Beijing National Laboratory for Molecular Sciences, State Key Laboratory of Rare Earth Materials Chemistry and Applications, College of Chemistry and Molecular Engineering, Peking University, Beijing 100871, P. R. China. E-mail: gaosong@pku.edu.cn*

† Electronic supplementary information (ESI) available. CCDC 2054834 and 2054835. For ESI and crystallographic data in CIF or other electronic format see DOI: 10.1039/d1sc01871j

‡ These authors contributed equally to this work.

Based on the work on targeted design strategies for molecular ferroelectrics,[44] herein, we successfully design a new organic–inorganic hybrid multiferroic, trimethylchloromethylammonium chromium chloride (TMCM–$CrCl_3$), which simultaneously shows excellent ferroelectricity and antiferromagnetism. Its paraelectric–ferroelectric transition at 397 K is related to the disorder–order transition of TMCM cations, and the magnetism is from the $[CrCl_3]^-$ framework. Notably, the observed C–Cl···Cl–Cr interactions between organic and inorganic components in TMCM–$CrCl_3$ play an important role in ensuring and stabilizing its polar organic–inorganic hybrid structure and ferroelectricity. To our knowledge, TMCM–$CrCl_3$ is the first experimentally confirmed Cr^{2+}-based multiferroic material, and also is the first Cr^{2+}-based organic–inorganic hybrid perovskite ferroelectric material. This work expectedly sheds light on the design of new multiferroic materials and inspires further exploration of the connection between the structure and properties.

Results and discussion

The crystal of TMCM–$CrCl_3$ adopts a $BaNiO_3$-like hexagonal perovskite structure, where infinite linear chains of face-sharing $CrCl_6$ octahedra are separated by the TMCM cations (Fig. 1 and ESI, Fig. S1†), analogous to several other ABX_3-type hybrid perovskites. In a low-temperature phase (LTP) below a Curie temperature (T_c) of 397 K, TMCM–$CrCl_3$ crystallizes in the monoclinic polar space group P_c (ESI, Table S1†). The structure in LTP was refined as an ordered state with distorted $[CrCl_6]$ octahedra. Fig. 1 depicts the structure of $3d^4$ $[CrCl_3]^-$ ions, which is the source of magnetism in the lattice. Structurally, TMCM cations adopt a manner of head-to-tail alignment along the *a*-axis, and the directions of C–Cl bonds are skewed toward the *c*-axis (Fig. 1a). The short intermolecular Cl···Cl contacts (3.236 and 3.243 Å) lead to the formation of C–Cl···Cl–Cr halogen bonds (bond angles of 177.07° and 173.79°) (ESI, Fig. S2†). Besides the size and weight of the molecule, the relatively strong halogen bonds play an important role in the cationic alignment, crystal symmetry and the potential energy barrier of molecular motion. These attributes make TMCM cations arrange in an orderly manner, resulting in a non-centrosymmetric structure and consequential spontaneous polarization. Additionally, because the $[CrCl_3]^-$ chains are separated by TMCM cations, intra-chain Cr···Cr distances are 3.309 Å and 3.335 Å, while the shortest inter-chain Cr···Cr distance reaches 9.069 Å (ESI, Fig. S3a†), which will lead to strong intra-chain Cr···Cr magnetic couplings and weak inter-chain Cr···Cr ones.

In the high-temperature phase (HTP, above T_c), the crystal structure of TMCM–$CrCl_3$ transforms to locating in the hexagonal centrosymmetric space group $P6_3/m$ (ESI, Table S1†). The configuration of $[CrCl_3]^-$ chains is similar to that of LTP, while the $CrCl_6$ octahedra become more regular (Fig. 1b), and the shortest intra/inter-chain Cr···Cr distances are 3.327 Å and 9.406 Å, respectively (ESI, Fig. S3b†). For the TMCM cation, its symmetry site changes from a general position in LTP to a special one of $\bar{6}/m$ (Fig. 1c and d), and thus the cations were modeled as 6-fold orientational disorder to satisfy the crystallographic symmetries. In HTP, the head-to-head and tail-to-tail alignments of TMCM cations lead to a centrosymmetric structure. Therefore, the paraelectric–ferroelectric phase transition mechanism can be attributed to the disorder–order transition of TMCM cations. The ferroelectricity is induced by the orientational ordering of TMCM cations, and the magnetism results from the transition metal $3d^4$ CrII ions.

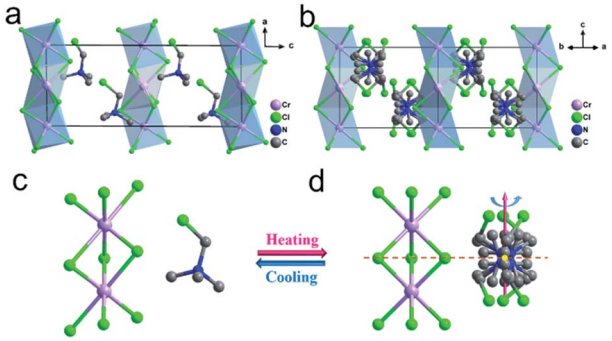

Fig. 1 Crystal structures of TMCM–$CrCl_3$. Packing view of a structure in (a) LTP and (b) HTP. (c) Structural unit in LTP, showing a distorted $[CrCl_6]$ octahedron and ordered TMCM cations. (d) Structural unit in HTP, showing a regular $[CrCl_6]$ octahedron and orientationally disordered TMCM cations. The brown line represents the mirror plane perpendicular to the *c*-axis. The pink arrow indicates the 6-fold rotoinversion axis. The yellow point represents the inversion center. H atoms were omitted for clarity.

The phase transition behavior of TMCM–$CrCl_3$ was directly detected by differential scanning calorimetry (DSC) measurements. From DSC curves (Fig. 2a), two pairs of successive thermal anomalies are observed at 381/371 K and 397/386 K in the heating/cooling runs, both of which are too close together to be separated, and thus can be considered as only one phase transition at about 397 K. Known from curves, the enthalpy change ΔH of TMCM–$CrCl_3$ is about 4.2 J g^{-1}. According to the

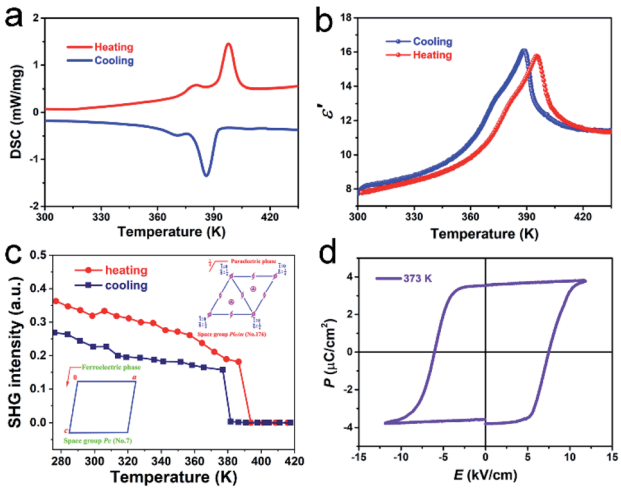

Fig. 2 Physical properties of TMCM–$CrCl_3$. (a) DSC curves in heating and cooling runs. (b) The real part (ε') of dielectric permittivity as a function of temperature. (c) Temperature-dependent SHG response in the heating and cooling runs. (d) *P*–*E* hysteresis loop measured along the polar axis of LTP at 373 K and 50 Hz.

formula $\Delta S = \Delta H/T$, the entropy change ΔS of the phase transition is calculated to be 5.6 J mol^{-1} K^{-1}. The calculated N value is 1.97 around T_c based on the Boltzmann equation $\Delta S = R\ln(N)$, where R represents the gas constant and N stands for the possible orientation number. Such a large N value reveals that the compound has a reversible transition between ordered and disordered states. Meanwhile, the real part (ε') of the dielectric permittivity of TMCM–$CrCl_3$ shows corresponding dielectric anomalies (Fig. 2b), consistent with the DSC result and further confirming the existence of a phase transition at a T_c of 397 K. We also performed the second harmonic generation (SHG) experiment to investigate the phase transition behaviour. As shown in Fig. 2c, TMCM–$CrCl_3$ displays a clear SHG at room temperature. In the heating and cooling runs, the detectable SHG response below T_c demonstrates the polar space group P_c in the ferroelectric phase. Near T_c, the sudden vanishing of the SHG response means that it enters into an SHG non-active state, in good agreement with the centrosymmetric 6/m point group in the paraelectric phase. In this case, symmetry breaking occurs with an Aizu notation of 6/mFm,[45] accompanied by a decrease in macroscopic symmetry elements from 12 (E, $2C_6$, $2C_3$, C_2, i, $2S_3$, $2S_6$, and σ_h) in the paraelectric phase to 2 (E and σ_h) in the ferroelectric phase. Accordingly, TMCM–$CrCl_3$ is a multiaxial ferroelectric with 6 equivalent polarization directions, corresponding to 3 ferroelectric axes.

To examine the ferroelectricity of TMCM–$CrCl_3$, we measured the polarization–electric field (P–E) hysteresis loop by using the Sawyer–Tower method at 298 K (Fig. 2d). A typical well-shaped P–E hysteresis loop was recorded, directly confirming the ferroelectricity of TMCM–$CrCl_3$. The measured saturated polarization (P_s) and remnant polarization (P_r) are almost equal, about 3.6 μC cm^{-2}, compared to that of TMCM–$CdBr_3$ (3.5 μC cm^{-2}),[46] and larger than those of other organic–inorganic hybrid multiferroics such as $(NH_4)_3CrO_8$ (0.25 μC cm^{-2}),[35] triethylmethylammonium tetrabromoferrate(III) (0.9 μC cm^{-2}),[34] and $[NH_4][M(HCOO)_3]$ (M = Mn, Fe, Co, Ni, and Zn) (0.97–2.2 μC cm^{-2}).[31]

In order to gain deep insight into the ferroelectric polarization, density functional theory (DFT) calculation was carried out to evaluate the origin of polarization.[43,47] According to the modern theory of polarization,[48,49] the necessity of constructing a polarization change path lies in selecting polarization quantum properly to avoid the wrong estimation of the polarization value. A dynamic path between ferroelectric and reference states is constructed based on the crystal structure obtained from single crystal X-ray diffraction, while the other states are obtained from the matrix transformation of the coordinates considering both the rotation of the TMCM cations and displacement of the anionic $CrCl_3$ framework. The variation of polarization as a function of the dynamic path is shown in ESI, Fig. S4,† from which the ferroelectric polarization with 4.82 μC cm^{-2} along the a-axis and 3.37 μC cm^{-2} along the c-axis can be extracted from the ferroelectric configurations ($\lambda = 1$). Meanwhile the polarization along the b-axis is zero, which is in good accordance with the symmetry of the space group P_c. Along with the constructed path ($0 < \lambda < 1$), the polarization value changes smoothly, and turns to zero at $\lambda = 0$, which indicates a reference phase with zero polarization.

The structure of TMCM–$CrCl_3$ consists of $[CrCl_3]^-$ anionic chains and TMCM cations. The $[CrCl_3]^-$ chain is made of 4 + 2 elongated $[CrCl_6]$ octahedra by face-sharing, and the chains are separated by the TMCM cations (detailed molecular geometries have been discussed above, such as intra/inter-chain Cr⋯Cr distances). Therefore, it is expected that the intra-chain Cr⋯Cr magnetic couplings will be strong, and the inter-chain Cr⋯Cr ones will be weak. Indeed, the material is a spin-canted antiferromagnetic with strong intra-chain antiferromagnetic coupling. Under a 100 Oe field, the χ *vs.* T data showed broad maxima around 70 K ($=T(\chi_{max})$) caused by strong intra-chain antiferromagnetic coupling (Fig. 3a). Below 15 K the trace rose up quickly. On cooling, the χT values continuously went down from 1.94 cm^3 K mol^{-1} at 300 K to 0.13 cm^3 K mol^{-1} around 7 K, and then rose to a maximum of 0.37 cm^3 K mol^{-1} at 4.0 K, and finally reached 0.25 cm^3 K mol^{-1} at 2 K. In higher fields of 2 and 10 kOe, the χT rises below 7 K were suppressed. This indicated the occurrence of spin-canted antiferromagnetism or weak ferromagnetism in the low-temperature region. Fitting the high-temperature susceptibility data (above 200 K and under 100 Oe) by the Curie–Weiss law (ESI, Fig. S5†), the Curie and Weiss constants could be obtained, C = 3.30 cm^3 K mol^{-1} and θ = −209 K, respectively. The C value is expected for octahedral CrII with $S = 2$,[50] and the large, negative θ value indicates strong intra-chain Cr⋯Cr antiferromagnetic couplings. In fact, the significantly low χT value of 1.94 cm^3 K mol^{-1} (compared with 3.00 cm^3 K mol^{-1} for spin-only, un-coupled spins of $S = 2$) at room temperature is due to such strong intra-chain antiferromagnetic couplings. From Fig. 3b–d, the zero-field-cooling and field-cooling (ZFC/FC, with small magnetizations of a few cm^3 G mol^{-1}) runs, the isothermal magnetizations (with small H_C = 110 Oe, $M_R = 0.00133N_\beta$ and $M_{50kOe} = 0.191N_\beta$) and the frequency-independent peaks in ac susceptibility data (ESI,

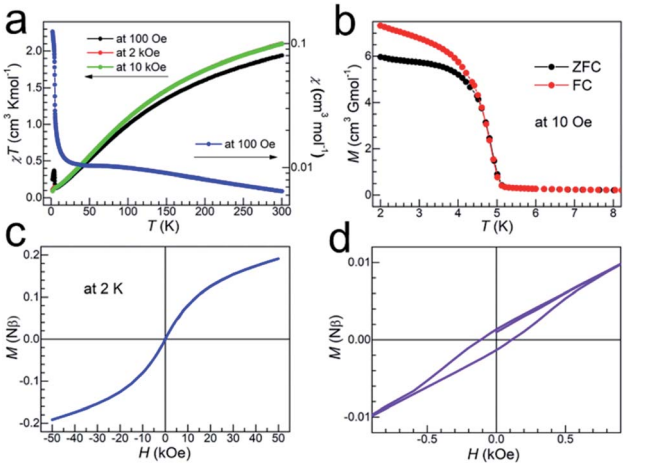

Fig. 3 Magnetic properties of TMCM–$CrCl_3$. (a) Temperature dependence of the magnetic susceptibility (χT). (b) Zero-field-cooling and field-cooling magnetization (M) under 10 Oe fields. (c) Field-dependent isothermal magnetization (M) at 2 K. (d) The zoomed views of magnetic hysteresis from (c).

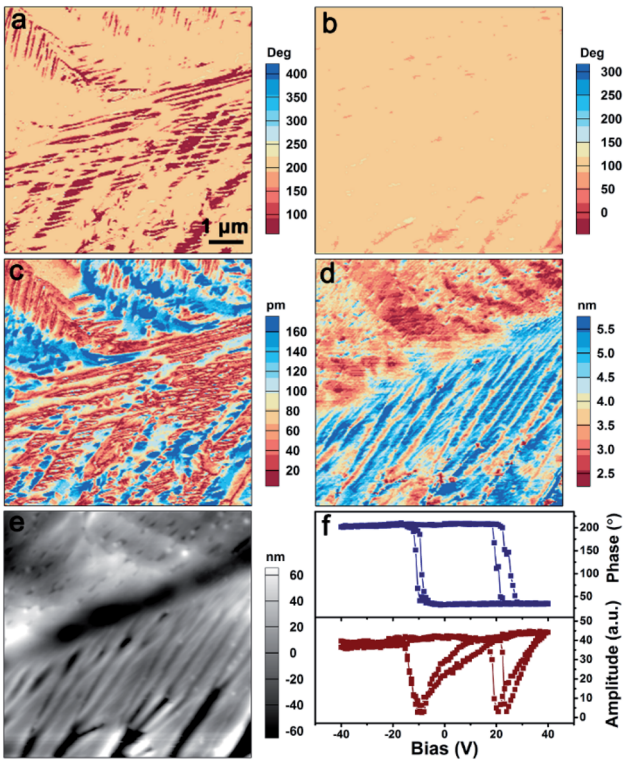

Fig. 4 Vertical PFM phase (a) and amplitude (c) images, lateral PFM phase (b) and amplitude (d) images, and topography (e) image of the thin film of TMCM–$CrCl_3$. (f) Vertical PFM phase and amplitude signals *versus* the tip voltage for a selected point, displaying local piezoelectric hysteresis loops.

Fig. S6†) all confirmed the spin-canted antiferromagnetic orderings in the low temperature region. The Néel temperature (T_N) is 4.8 K, determined by ZFC/FC and ac measurements. Finally, the intra-chain Cr···Cr antiferromagnetic coupling J could be estimated to be $J/k \approx 10$ K, by using the equation of $kT(\chi_{max})/|J| \approx 7.1$,[51] assuming that the chain is of Heisenberg type with $S = 2$.

Next, piezoresponse force microscopy (PFM) measurements were performed as they represent the most well-known technique for elucidating the ferroelectric properties at the nanoscale. Fig. 4a–e show the PFM mapping of the as-grown TMCM–$CrCl_3$ thin film, including the vertical PFM phase (Fig. 4a) and amplitude (Fig. 4c), lateral PFM phase (Fig. 4b) and amplitude (Fig. 4d) images and the corresponding topographic image (Fig. 4e). It reveals that domains with different polarization directions exist in TMCM–$CrCl_3$. These polarizations have opposite out-of-plane directions but the same in-plane direction, as presented by the vertical and lateral PFM phase images. Thus, they are non-180° domains, which are permitted in the multiaxial TMCM–$CrCl_3$. The amplitude images present the magnitude of the piezoresponse of each domain, corresponding well to the phase image. When the piezoresponse is overlaid on the three-dimensional (3D) morphology, it can be seen that the phase and amplitude signals have no obvious correlation with the local topology of the film surface, which excludes the interference from topographic artifacts and further demonstrates the existence of the domain structure (ESI, Fig. S7†).

The switching spectroscopy approach based on PFM (SS-PFM) has been widely used to explore ferroelectric behaviors. SS-PFM is typically performed at a fixed point by applying a pulse-type triangular bias voltage waveform.[52] The hysteresis amplitude and phase loops can be obtained by applying a probing ac voltage while the dc voltage is in the off state. Fig. 4f shows the obtained PFM hysteresis loops as a function of dc voltage. The 180° shifting of the phase signal and the corresponding butterfly-shaped amplitude loop reveal the ferroelectric switching. Domain switching can also be performed with PFM as the PFM tip can be used as a movable top electrode for applying a voltage to the sample. Fig. S8 in the ESI† shows the PFM images before and after two step poling procedures. The 180° phase difference can be observed in the phase images when the upward (ESI, Fig. S8b,† −50 V) and the downward (ESI, Fig. S8c,† +30 V) polarization switching occur. The domain walls can be discerned in the corresponding amplitude images. Thus, the ferroelectricity of TMCM–$CrCl_3$ has been well characterized by PFM measurements.

Conclusions

In summary, our work demonstrates that magnetic and electric orderings coexist in a new organic–inorganic hybrid TMCM–$CrCl_3$, as the first case of a Cr^{2+}-based multiferroic material. It experiences a paraelectric–ferroelectric transition at 397 K with an Aizu notation of 6/*mFm*, triggered by a disorder–order transition of TMCM cations. The strong intra-chain $Cr^{II}\cdots Cr^{II}$ magnetic couplings indicate its spin-canted antiferromagnetism. These findings will open up a new avenue for multiferroic systems.

Experimental

Material synthesis and crystal growth

All reagents and solvents in this experiment were of reagent grade and used without further purification. Trimethylchloromethylammonium chloride (TMCM·Cl) was synthesized by the reaction of equimolar amounts of trimethylamine (30 wt% in water) and dichloromethane in acetonitrile at 60 °C for 24 h. The solvent was removed under reduced pressure to obtain a colorless solid. TMCM–$CrCl_3$ was prepared by dissolving equimolar amounts of TMCM·Cl and chromium(II) chloride in hot ethanol solution under stirring. Colorless needle-like single crystals were grown by slow evaporation of the clear solution in a glove box. All the experimental measurements of TMCM–$CrCl_3$ were conducted under a nitrogen atmosphere. The PXRD pattern obtained at 293 K matches well with the result simulated from the single-crystal structure (ESI, Fig. S9†), unraveling the high crystallinity and phase purity. Elemental analysis, calcd (%) for TMCM–$CrCl_3$: C, 18.00; N, 5.25; H, 4.15. Found: C, 18.45; N, 5.43; H, 4.25.

Thin-film preparation

The precursor solution of TMCM–$CrCl_3$ was prepared by dissolving 30 mg of crystals in 300 μL of ethanol. Then, 20 μL of

precursor solution was spread on a clean indium-doped tin oxide (ITO) glass substrate (1 × 1 cm). The thin films of TMCM–$CrCl_3$ were obtained after evaporating solution at room temperature for 30 min. These thin films were used for *P–E* hysteresis loop and PFM measurements.

X-ray diffraction characterization

Single-crystal X-ray diffraction data were measured using a Rigaku Varimax™ DW diffractometer with Mo-Kα radiation (λ = 0.71073 Å). The structures were solved by direct methods and refined by the full-matrix method based on F^2 using the SHELXTL software package. All non-hydrogen atoms were refined anisotropically and the positions of all hydrogen atoms were generated geometrically. The data collection and structure refinement of these crystals are summarized in ESI, Table S1.† The X-ray crystallographic structures have been deposited at the Cambridge Crystallographic Data Centre (deposition numbers CCDC: 2054834 and 2054835) and can be obtained free of charge from the CCDC *via* www.ccdc.cam.ac.uk/getstructures. Powder X-ray diffraction (PXRD) data were measured using a Rigaku D/MAX 2000 PC X-ray diffraction system with Cu Kα radiation in the 2θ range of 5°–50° with a step size of 0.02° and a scan rate of 10° min^{-1}.

Magnetic measurements

Magnetic measurements for the compound were performed on a Quantum Design MPMSXL5 SQUID system with polycrystalline samples. The samples were first wrapped with N-grease and a film, tightly packed and sealed in a capsule, and then installed firmly in a straw. The above procedure of sample preparation for magnetic study was carried out under an Ar atmosphere in a glove box, and then the package was brought to the instrument site in a sealed vessel filled with Ar, and finally transferred into the chamber of a SQUID system (in a He atmosphere) within one minute. After magnetic measurements, the samples showed no change in the color and morphology. Therefore, we believe that the samples were well protected. Diamagnetic corrections were estimated using Pascal constants for the compound and the background corrections by experimental measurements on sample holders (N-grease, film and capsule used).

DSC, SHG and dielectric measurements

Differential scanning calorimetry (DSC) measurements were recorded on a NETZSCH DSC 200F3 instrument by heating and cooling crystalline samples with a rate of 20 K min^{-1} in aluminum crucibles under a nitrogen atmosphere. SHG measurements were carried out on an FLS 920, Edinburgh Instruments using an unexpanded laser beam with low divergence (pulsed Nd:YAG at a wavelength of 1064 nm). The laser is a Vibrant 355 II, OPOTEK. The complex dielectric permittivity curves were recorded on an automatic impedance Tonghui 2828 analyzer. Dielectric studies were performed on pressed-powder pellets, and conductive carbon glue was deposited on the surface of the electrode to simulate parallel plate capacitors.

Thermogravimetric analysis (TGA) measurement

The TGA measurement was performed by using a PerkinElmer TGA 8000. The decomposition temperature of TMCM–$CrCl_3$ is around 290 °C; see Fig. S10 in the ESI.†

Calculation conditions

In order to investigate the microscopic ferroelectric polarization, we carried out density functional calculations based on the Berry phase method developed by Kingsmith and Vanderbilt.[53,54] The first-principles calculations were performed within the framework of density functional theory implemented in the Vienna *ab initio* Simulation Package (VASP).[55,56] The energy cutoff for the expansion of the wave functions was fixed at 550 eV and the exchange–correlation interactions were treated within the generalized gradient approximation of the Perdew–Burke–Ernzerhof type.[57] For the integrations over the *k*-space we used a 4 × 3 × 2 *k*-point mesh. The experimental crystal structure was used as the ground state for evaluating the ferroelectric polarization. The rotation of the TMCM cations and the displacement of the $CrCl_3$ framework are realized by matrix transformation of the coordinates using Microsoft Excel.

Author contributions

Ren-Gen Xiong and Song Gao devised and developed the project. Yong Ai and Rong Sun performed the experiments. All the authors analysed the data, discussed the results and participated to the manuscript.

Conflicts of interest

There are no conflicts to declare.

Acknowledgements

This work was financially supported by the National Natural Science Foundation of China (21991140 and 21831004).

Notes and references

1 S. Horiuchi and Y. Tokura, *Nat. Mater.*, 2008, **7**, 357–366.
2 P.-F. Li, W.-Q. Liao, Y.-Y. Tang, W. Qiao, D. Zhao, Y. Ai, Y.-F. Yao and R.-G. Xiong, *Proc. Natl. Acad. Sci. U. S. A.*, 2019, **116**, 5878–5885.
3 C. Qiu, B. Wang, N. Zhang, S. Zhang, J. Liu, D. Walker, Y. Wang, H. Tian, T. R. Shrout and Z. Xu, *Nature*, 2020, **577**, 350–354.
4 J. Scott, *science*, 2007, **315**, 954–959.
5 C. Shi, L. Ye, Z.-X. Gong, J.-J. Ma, Q.-W. Wang, J.-Y. Jiang, M.-M. Hua, C.-F. Wang, H. Yu and Y. Zhang, *J. Am. Chem. Soc.*, 2019, **142**, 545–551.
6 Y.-M. You, W.-Q. Liao, D. Zhao, H.-Y. Ye, Y. Zhang, Q. Zhou, X. Niu, J. Wang, P.-F. Li and D.-W. Fu, *Science*, 2017, **357**, 306–309.
7 M. Bichurin, V. Petrov, S. Priya and A. Bhalla, *Adv. Condens. Matter Phys.*, 2012, **2012**, 129794.

8 W. Eerenstein, N. Mathur and J. F. Scott, *Nature*, 2006, **442**, 759–765.
9 J. Scott, *Nat. Mater.*, 2007, **6**, 256–257.
10 L. Ju, T. Sabergharesou, K. G. Stamplecoskie, M. Hegde, T. Wang, N. A. Combe, H. Wu and P. V. Radovanovic, *J. Am. Chem. Soc.*, 2012, **134**, 1136–1146.
11 C.-Y. Kuo, Z. Hu, J. Yang, S.-C. Liao, Y. Huang, R. Vasudevan, M. Okatan, S. Jesse, S. V. Kalinin and L. Li, *Nat. Commun.*, 2016, **7**, 1–7.
12 S. A. Larregola, J. C. Pedregosa, M. Algueró, R. Jiménez, M. García-Hernandez, M. T. Fernandez-Diaz and J. A. Alonso, *Chem. Mater.*, 2012, **24**, 2664–2672.
13 H. Liu and X. Yang, *Ferroelectrics*, 2017, **507**, 69–85.
14 J. Wang, J. Neaton, H. Zheng, V. Nagarajan, S. Ogale, B. Liu, D. Viehland, V. Vaithyanathan, D. Schlom and U. Waghmare, *Science*, 2003, **299**, 1719–1722.
15 T. Kimura, S. Kawamoto, I. Yamada, M. Azuma, M. Takano and Y. Tokura, *Phys. Rev. B*, 2003, **67**, 180401.
16 N. Hur, S. Park, P. Sharma, J. Ahn, S. Guha and S.-W. Cheong, *Nature*, 2004, **429**, 392–395.
17 M. Fiebig, T. Lottermoser, D. Fröhlich, A. V. Goltsev and R. V. Pisarev, *Nature*, 2002, **419**, 818–820.
18 S.-W. Cheong and M. Mostovoy, *Nat. Mater.*, 2007, **6**, 13–20.
19 N. A. Hill, *J. Phys. Chem. B*, 2000, **104**, 6694–6709.
20 V. B. Lu, F. M. Gribble and F. Reimann, *Nutrients*, 2021, **13**, 883.
21 Y. Shen, G. Cosquer, H. Ito, D. C. Izuogu, A. J. Thom, T. Ina, T. Uruga, T. Yoshida, S. Takaishi and B. K. Breedlove, *Angew. Chem., Int. Ed.*, 2020, **132**, 2420–2427.
22 T. Hang, W. Zhang, H.-Y. Ye and R.-G. Xiong, *Chem. Soc. Rev.*, 2011, **40**, 3577–3598.
23 P.-P. Shi, Y.-Y. Tang, P.-F. Li, W.-Q. Liao, Z.-X. Wang, Q. Ye and R.-G. Xiong, *Chem. Soc. Rev.*, 2016, **45**, 3811–3827.
24 W. Zhang and R.-G. Xiong, *Chem. Rev.*, 2012, **112**, 1163–1195.
25 B. Huang, J.-Y. Zhang, R.-K. Huang, M.-K. Chen, W. Xue, W.-X. Zhang, M.-H. Zeng and X.-M. Chen, *Chem. Sci.*, 2018, **9**, 7413–7418.
26 W. Li, Z. Wang, F. Deschler, S. Gao, R. H. Friend and A. K. Cheetham, *Nat. Rev. Mater.*, 2017, **2**, 1–18.
27 B. Saparov and D. B. Mitzi, *Chem. Rev.*, 2016, **116**, 4558–4596.
28 G.-C. Xu, X.-M. Ma, L. Zhang, Z.-M. Wang and S. Gao, *J. Am. Chem. Soc.*, 2010, **132**, 9588–9590.
29 D. W. Fu, W. Zhang, H. L. Cai, Y. Zhang, J. Z. Ge, R. G. Xiong, S. D. Huang and T. Nakamura, *Angew. Chem., Int. Ed.*, 2011, **50**, 11947–11951.
30 L. C. Gómez-Aguirre, B. n. Pato-Doldán, J. Mira, S. Castro-García, M. A. Señarís-Rodríguez, M. Sánchez-Andújar, J. Singleton and V. S. Zapf, *J. Am. Chem. Soc.*, 2016, **138**, 1122–1125.
31 G.-C. Xu, W. Zhang, X.-M. Ma, Y.-H. Chen, L. Zhang, H.-L. Cai, Z.-M. Wang, R.-G. Xiong and S. Gao, *J. Am. Chem. Soc.*, 2011, **133**, 14948–14951.
32 D. Di Sante, A. Stroppa, P. Jain and S. Picozzi, *J. Am. Chem. Soc.*, 2013, **135**, 18126–18130.
33 A. Stroppa, P. Jain, P. Barone, M. Marsman, J. M. Perez-Mato, A. K. Cheetham, H. W. Kroto and S. Picozzi, *Angew. Chem., Int. Ed.*, 2011, **50**, 5847–5850.
34 H.-L. Cai, Y. Zhang, D.-W. Fu, W. Zhang, T. Liu, H. Yoshikawa, K. Awaga and R.-G. Xiong, *J. Am. Chem. Soc.*, 2012, **134**, 18487–18490.
35 R. Samantaray, R. J. Clark, E. S. Choi and N. S. Dalal, *J. Am. Chem. Soc.*, 2012, **134**, 15953–15962.
36 R. Samantaray, R. J. Clark, E. S. Choi, H. Zhou and N. S. Dalal, *J. Am. Chem. Soc.*, 2011, **133**, 3792–3795.
37 M. Maczka, K. Pasinska, M. Ptak, W. Paraguassu, T. A. da Silva, A. Sieradzki and A. Pikul, *Phys. Chem. Chem. Phys.*, 2016, **18**, 31653–31663.
38 M. Maczka, A. Gagor, M. Ptak, W. Paraguassu, T. A. da Silva, A. Sieradzki and A. Pikul, *Chem. Mater.*, 2017, **29**, 2264–2275.
39 Z. Hu, H. Zhao, Z. Cheng, J. Ding, H. Gao, Y. Han, S. Wang, Z. Xu, Y. Zhou, T. Jia, H. Kimura and M. Osada, *Phys. Chem. Chem. Phys.*, 2020, **22**, 4235–4239.
40 J. M. Bermudez-Garcia, M. Sanchez-Andujar, S. Castro-Garcia, J. Lopez-Beceiro, R. Artiaga and M. A. Senaris-Rodriguez, *Nat. Commun.*, 2017, **8**, 15715.
41 J. P. Zhao, J. Xu, S. D. Han, Q. L. Wang and X. H. Bu, *Adv. Mater.*, 2017, **29**, 1606966.
42 L. Canadillas-Delgado, O. Fabelo, J. A. Rodriguez-Velamazan, A. Stunault, J.-P. Zhao, X.-H. Bu and J. Rodriguez-Carvajal, *Iucrj*, 2020, **7**, 803–813.
43 A. Stroppa, P. Barone, P. Jain, J. M. Perez-Mato and S. Picozzi, *Adv. Mater.*, 2013, **25**, 2284–2290.
44 H.-Y. Liu, H.-Y. Zhang, X.-G. Chen and R.-G. Xiong, *J. Am. Chem. Soc.*, 2020, **142**, 15205–15218.
45 K. Aizu, ecirc and itsiro, *J. Phys. Soc. Jpn.*, 1969, **27**, 387–396.
46 W.-Q. Liao, Y.-Y. Tang, P.-F. Li, Y.-M. You and R.-G. Xiong, *J. Am. Chem. Soc.*, 2018, **140**, 3975–3980.
47 D. Di Sante, A. Stroppa, P. Jain and S. Picozzi, *J. Am. Chem. Soc.*, 2013, **135**, 18126–18130.
48 N. A. Spaldin, *J. Solid State Chem.*, 2012, **195**, 2–10.
49 R. Resta and D. Vanderbilt, *Physics of Ferroelectrics: A Modern Perspective* 2007, vol. 105, pp. 31–68.
50 E. A. Boudreaux and L. Mulay, *Theory and applications of molecular paramagnetism*, John Wiley & Sons, 1976.
51 W. Haase, *Bunsen-Ges. Phys. Chem., Ber.*, 1988, **92**, 453.
52 O. Kwon, D. Seol, H. Qiao and Y. Kim, *Adv. Sci.*, 2020, **7**, 1901391.
53 R. King-Smith and D. Vanderbilt, *Phys. Rev. B*, 1993, **47**, 1651.
54 D. Vanderbilt and R. King-Smith, *Phys. Rev. B*, 1993, **48**, 4442.
55 G. Kresse and J. Furthmüller, *Phys. Rev. B*, 1996, **54**, 11169.
56 G. Kresse and J. Furthmüller, *Comput. Mater. Sci.*, 1996, **6**, 15–50.
57 J. P. Perdew, K. Burke and M. Ernzerhof, *Phys. Rev. Lett.*, 1996, **77**, 3865–3868.